Steering the synthesis of Fe_3O_4 nanoparticles under sonication by using a fractional factorial design

J. C. Echeverría* [1,2], P. Moriones[1,2], J.J. Garrido[1,2], M.D. Ugarte[2,3], L. Cervera[1,2], E. Garaio[1,2], C. Gómez-Polo[1,2], J.I. Pérez-Landazábal[1,2]

[1]*Departamento de Ciencias, Universidad Pública de Navarra, 31006 Pamplona, Spain*

[2]*Institute for Advanced Materials and Mathematics (INAMAT[2]), Universidad Pública de Navarra, 31006 Pamplona, Spain*

[3]*Departamento de Estadística, Informática y Matemáticas, Universidad Pública de Navarra, 31006 Pamplona, Spain*

Highlights

- The coprecipitation pathway depended on the initial concentration of Fe.
- SAR was highest for samples obtained from 0.110 mol L^{-1} Fe, in 0.90 mol L^{-1} $NH_{3(aq)}$, sonicated for 1 h.
- Sonication of the reaction mixture boosted phase transformation to magnetite.
- Fractional factorial designs are a powerful tool for steering the synthesis of Fe_3O_4 MNPs.

Graphical Abstract

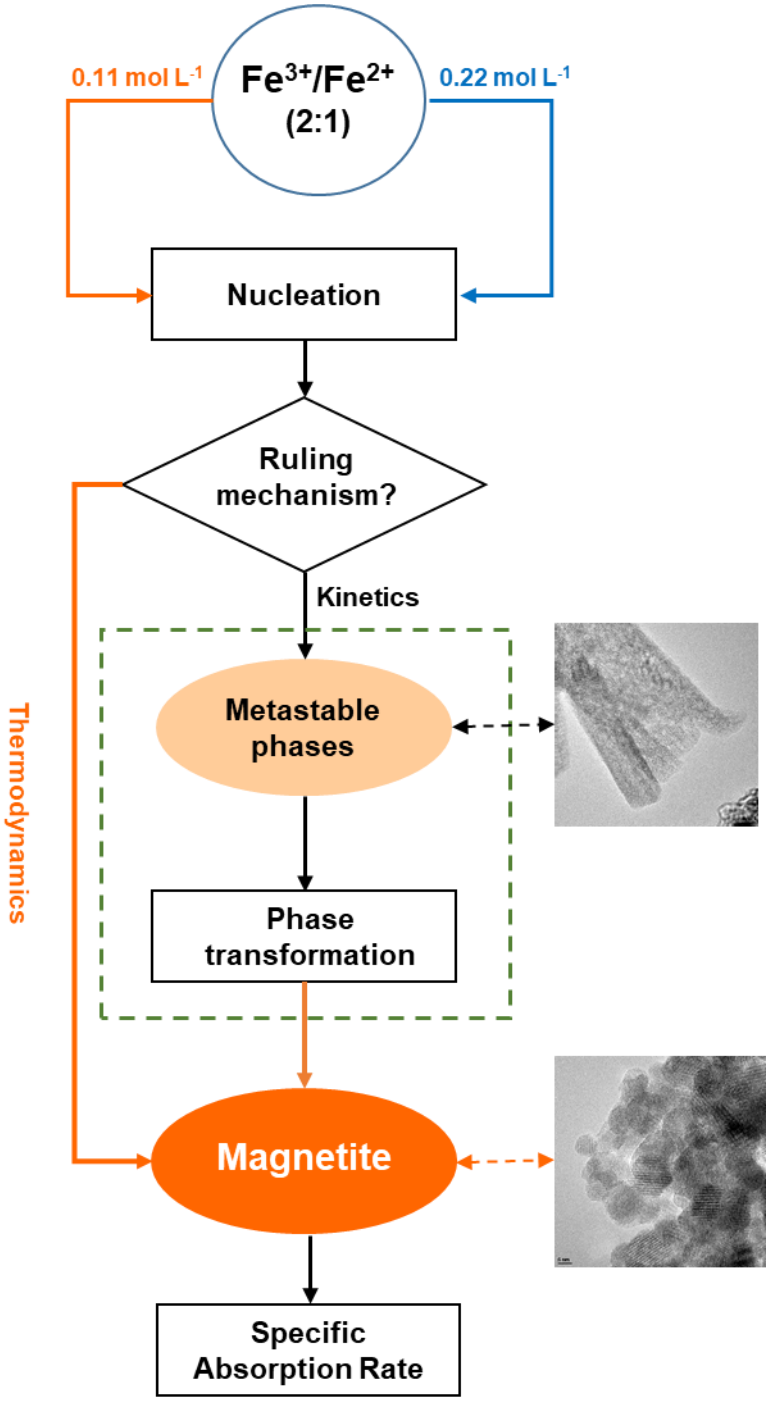

Abstract

Superparamagnetic iron oxide nanoparticles (MNPs) have the potential to act as heat sources in magnetic hyperthermia. The key parameter for this application is the specific absorption rate (SAR), which must be as large as possible in order to optimize the hyperthermia treatment. We applied a Plackett-Burman fractional factorial design to investigate the total iron concentration, ammonia concentration, reaction temperature, sonication time and percentage of ethanol in the aqueous media on the properties of iron oxide MNPs. Characterization techniques included total iron content, Fourier Transform Infrared Spectroscopy, X-Ray Diffraction, High Resolution Transmission Electron Microscopy, and Dynamic Magnetization. The reaction pathway in the coprecipitation reaction depended on the initial Fe concentration. Samples synthesized from 0.220 mol L^{-1} Fe yielded magnetite and metastable precipitates of iron oxyhydroxides. An initial solution made up of 0.110 mol L^{-1} total Fe and either 0.90 or 1.20 mol L^{-1} $NH_{3(aq)}$ led to the formation of magnetite nanoparticles. Sonication of the reaction media promoted a phase transformation of metastable oxyhydroxides to crystalline magnetite, the development of crystallinity, and the increase of specific absorption rate under dynamic magnetization.

Keywords

Magnetite nanoparticles, Sonication, Specific absorption rate, Fractional factorial design, Phase transformation

1 Introduction

In recent years, superparamagnetic iron oxide magnetic nanoparticles (MNPs) have gained notoriety in the field of medicine thanks to their remarkable physical and chemical properties. Functionalized nanoparticles are biocompatible and, what is more, can target a specific type of cells by means of different biomarkers. Hence, they can be used in several imaging techniques such as MRI contrast agents [1] or as magnetic particle imaging tracers [1]. There also exist other potential applications in the field of biodetection of functionalized MNPs [2] and in the environment, namely, in catalysis and photocatalysis [3], and sensors [4].

Moreover, superparamagnetic MNPs have the potential to act as heat sources in magnetic hyperthermia, a "novel" cancer therapy [4]. MNPs placed inside or near a tumour absorb energy from an externally applied alternating magnetic field creating hyperthermia conditions only in the tumour, leaving the healthy tissues undamaged. For this application, the specific absorption rate (SAR), which is the power absorbed by the MNPs normalized by their mass [5], must be as large as possible in order to optimize the hyperthermia therapy. Therefore, a synthesis process for superparamagnetic MNPs intended for medical applications should pursue a maximization of the SAR. According to the literature, SAR depends on a wide variety of parameters [6-8], including chemical composition, the intrinsic magnetization, magnetic anisotropy, grain size, morphology, agglomeration rate and the medium.

Among the numerous methods that have been used to synthesize magnetic nanoparticles (MNPs) [9-11], the coprecipitation technique is perhaps the simplest and most efficient chemical way to obtain these nanoparticles. However, the synthesis of magnetic nanoparticles (i.e. Fe_3O_4 magnetite or γ-Fe_2O_3 maghemite) is not straightforward. The complexity of iron reactions in aqueous media arises from the occurrence of two oxidation states, which are stable in a large range of acidity, the high reactivity of iron complexes toward acid-base and condensation reactions [12], the colloidal nature of precipitates, and the formation of thermodynamically stable crystalline phases preceded by metastable intermediates.

During the coprecipitation synthesis, the nucleation and growth of MNPs are affected simultaneously by numerous parameters, such as total Fe concentration, the ratio of Fe(III) and Fe(II) precursors, the nature and concentration of the base, as well as the temperature [13-16]. The role of sonication in the synthesis of magnetite nanoparticles has received less attention. For instance, Meng et al.[14] reported the orthogonal optimization for the preparation of Fe_3O_4 nanoparticles via coprecipitation. These authors included ultrasonic dispersion in the synthesis but it was not included in the process parameters of the orthogonal experiments. Accordingly, we have included the effect of sonication time as a process variable in a Factorial Fractional Design to investigate the effect of the synthesis parameters on the composition, size and SAR of iron oxide magnetic nanoparticles. This approach reduces the number of experiments in a research project and provides information about interactions among variables [17]. Five

dummy variables were included to estimate the standard error and apply the t-test to determine the significant factors in the properties of the NPs.

The goal of this research was to assess the simultaneous effect of the synthesis variables on the composition, structure, morphology and specific absorption rate (SAR) of the iron oxide nanoparticles. To avoid fractional precipitation of iron oxyhydroxides, we added an acidified mixture of Fe(II) and Fe(III) salts to aqueous ammonia solutions. Because Fe(III) aquo complexes are more acidic than Fe(II) complexes, hydroxylation of Fe(III) cation occurs from pH 1 to 5 at room temperature, whereas hydroxylation of Fe(II) occurs in the range pH 7 – 9[12].

2 Material and experimental methods

2.1 Experimental design

We applied the Plackett-Burman fractional factorial design [18] to investigate the effect of the synthesis conditions on the composition and morphology of iron oxides magnetic nanoparticles. The experimental factors were chosen taking into account the theory of the homogenous nucleation and leading references in the synthesis of iron oxides [19-21]. The factors were the initial concentration of Fe(III) and Fe(II) (A), synthesis temperature (C), ethanol concentration in the aqueous solvent (E), ammonia concentration (G), sonication time (I) and drying temperature (K). We kept the molar ratio Fe(III)/Fe(II) equal to two [19], and purged the solutions with $N_{2(g)}$ to prevent the oxidation of Fe(II) ions. To measure the experimental error of the system and to improve the robustness of the design, we included five dummy factors (D1-D5). Consequently, we selected the design for 12 runs from the Plackett – Burman method [18]. Taking the simplest eleven-factor matrix, at two levels, the final matrix was constructed as shown in Table 1. The coded levels of each factor are shown in Table 2 and the experimental conditions for each run are included in Table ESI1 of Electronic Supplementary Information.

Table 1 Final matrix for a Plackett – Burman design for eleven factors and twelve runs.

Experiment number	Fe total conc.	D1	Synthesis temperature	D2	Ethanol content	D3	Ammonia concentration	D4	Sonication time	D5	Drying temperature
	A	**B**	**C**	**D**	**E**	**F**	**G**	**H**	**I**	**J**	**K**
1	+	+	-	+	+	+	-	-	-	+	-
2	-	+	+	-	+	+	+	-	-	-	+
3	+	-	+	+	-	+	+	+	-	-	-
4	-	+	-	+	+	-	+	+	+	-	-
5	-	-	+	-	+	+	-	+	+	+	-
6	-	-	-	+	-	+	+	-	+	+	+
7	+	-	-	-	+	-	+	+	-	+	+
8	+	+	-	-	-	+	-	+	+	-	+
9	+	+	+	-	-	-	+	-	+	+	-
10	-	+	+	+	-	-	-	+	-	+	+
11	+	-	+	+	+	-	-	-	+	-	+
12	-	-	-	-	-	-	-	-	-	-	-

Although the Fe(III) / Fe(II) ratio was kept equal to two, we changed the initial concentration because it can affect the degree of supersaturation for precipitation to occur. The precipitation temperature also affects supersaturation, the critical radius and the activation energy maximum which, in turn, control the nucleation rate. The surface tension of the solvent was modified by changing the ethanol content in the aqueous solution. The ammonia concentration was modified to take into account the effect on the precipitation and stability of colloids. Sonication time and drying temperature can affect the phase transformation and stability of the nanoparticles.

Table 2 Experimental factors and coded levels.

Factor	Level	
	–	+
Total Fe concentration (M). Fe(III)/Fe(II) ratio was 2:1.	0.110	0.220
Reaction temperature (ºC)	30	50
Content of ethanol in the aqueous solution (%)	5	25
Ammonia concentration in the aqueous solution (M)	1.2	0.90
Sonication time (min)	10	60
Drying temperature under vacuum (ºC)	60	105

2.2 Synthesis

First, 50 mL of aqueous 0.90 or 1.2 mol L^{-1} ammonia aqueous solution, containing either 5 or 25 % (v/v) ethanol, were prepared in calibrated flasks. Each solution was transferred to a 50 mL centrifuge tube in order to limit the loss of matter and the oxidation of nanoparticles. The pH of ammonia solutions was 10.0 for 0.90 mol L^{-1} and 12.1 for 1.2 M. Each solution was heated to 30 or 50 ºC (IKA® C- MAG HS-7; IKA® ETS-D5), and kept under a purge of nitrogen to displace dissolved oxygen.

In parallel, 1.092 g or 2.180 g of $FeCl_3 \cdot 6H_2O$ (purity ≥ 99%, Sigma-Aldrich), as well as 0.5616 or 1.123 g of $FeSO_4 \cdot 7H_2O$ (purity ≥ 99%, Sigma-Aldrich), were weighed and mixed. The mixture of salts was dissolved in 5 mL of 2.0 mol L^{-1} HCl under a nitrogen purge to reduce the oxidation of Fe(II) ions. Despite the purge with $N_{2(g)}$, the solution with a larger concentration of salts changed from orange to a brownish colour.

When the temperature of the ammonia solution was stabilized at either 30 or 50 ºC, we immersed the ultrasound probe into the solution and added the whole volume of the iron salt solution. Therefore, the total concentration of iron was 0.220 mol L^{-1} and 0.110 mol L^{-1} for the

largest and lowest concentration, respectively. Depending on the specific concentrations, a black or a black-brownish precipitate was obtained. The samples were sonicated for 10 or 60 min. Then they were centrifuged at 4000 rpm for 15 min (Hermle Z-320), the supernatant was discarded and the residue was washed twice with 10-mL aliquots of MiliQ water purged with nitrogen. The powders were dried either at 60 or 105 ºC, in a desiccator under vacuum (Vacuo-Temp Selecta 4000474 connected to an Adixen Pascal 2005SD vacuum pump). Samples are denoted in the manuscript with the initial and the run number from S1 to S12.

2.3 Characterization techniques

The total content of iron in the dried samples was measured by using atomic absorption spectrometry. Approximately 10 mg of the sample was added to 4 mL of 1:1 HCl (37%) aqueous solution and the mixture was heated until the solids dissolved. Then the solution was transferred to a calibrated flask of 100 mL and water was added to the final volume. The calibration line up to 5 mg L^{-1} was prepared from a 1.000 g L^{-1} standard solution of Fe.

FTIR spectra were obtained with a Nicolet Avatar 360 FT-IR spectrometer in the range 400 – 4000 cm^{-1} using KBr pellets. Each spectrum was the result of accumulating 32 scans with a spectral resolution of 2 cm^{-1}. In order to avoid saturating the detector and to optimize the comparison between samples, 0.60 mg of each sample was dispersed in 199.4 mg of KBr. The pellets were kept at 423 K for 2 h to minimize the amount of adsorbed water. To gain detail in the spectral region 400 – 800 cm^{-1}, where the specific bands for Fe – O stretching are found, we applied the finite-difference computation as an approximation to the second derivative [22, 23]. In order to improve the signal-to-noise ratio and to avoid artifact peaks, 20 cm^{-1} was chosen as the wavelength spacing for calculating the finite-differences in the absorption spectra.

The x-ray powder diffraction patterns were recorded at room temperature on a Siemens D-5000 diffractometer equipped with a graphite monochromator and a copper anode. The diffractometer operated at 30 mA and 40 kV. XRD data were collected at diffraction angles between 10 and 80 º, the operating speed was 0.02 º s^{-1} and the integration time was 20 s. Crystallite size was measured by applying the Debye-Scherrer approximation.

High resolution transmission electron microscopy (HRTEM) and scanning transmission electron microscopy with a high angle annular dark field detector (STEM-HAADF) analysis were performed by using a FEI Tecnai Field Emission Gun (Germany) operated at 300 kV.

Finally, the specific absorption rate (*SAR*) was obtained from the AC hysteresis loop area according to the following expression:

$$SAR = -\mu_0 \int M_t \, dH_{AC}$$

where M_t is the time dependent dynamic magnetization (normalized by MNP mass) and H_{AC} is the externally applied magnetic field intensity. A resonant LCC circuit fed by an RF power

amplifier (Electronic & Innovation, mod. 1240 L) generated the external magnetic field, while the dynamic M_t magnetization was measured by an AC magnetometry pick-up coil system [24]. The AC magnetic field frequency was 284 kHz, whereas the field intensity was increased to 32 kA/m (400 Oe). The dynamic magnetizations were measured with the MNPs samples dispersed in glycerol.

3 RESULTS AND DISCUSSION

3-1 Total iron content

The total content of iron, expressed as a percentage of dry matter, varied from 50% for samples S1 and S3 to 72.5% for sample S4. Eight from twelve samples had an Fe percentage higher than 67.5%. Figure 1(a) shows the average value of the total content of iron for each sample and the standard deviation of the experimental characterization (in a three-dimensional experimental space that includes the total iron concentration, the sonication time and the drying temperature under vacuum). The initial concentration of Fe(III) a Fe(II) in the initial mixture and the sonication time significantly affected the iron content. The lowest percentages of iron were for the samples synthesized from 0.220 mol L^{-1} Fe, which were sonicated for 10 min (S1, S3 and S7). For a 0.110 mol L^{-1} Fe concentration, the six samples had Fe percentages higher than 68%, which are slightly lower than the Fe percentages for Fe_2O_3 (69.9%) and Fe_3O_4 (72.4%). For samples synthesized at higher concentrations of Fe(III) and Fe(II), increasing the sonication time from 10 to 60 min resulted in samples with a larger Fe content. These results point to a phase transformation promoted by sonication. Table ESI2 shows the estimated effect of the experimental variables on the Fe content of the samples and the evaluated t-test. A brief description of the statistical analysis is also included. As can be seen, the initial Fe content (A) and the sonication times (I) appear to have a significant effect on the final Fe content of the samples. To further analyse these effects, Figure 1(b) shows a half-probability plot employing the estimated t-test of the six experimental variables plus the data associated with the 5 dummies. With the exception of the final Fe concentration and the sonication time, the rest of the variables fall on a straight line passing through the origin (zero). It should be borne in mind that this straight line is an accumulative distribution and that the variables falling on the line show a normally distributed random error effect.

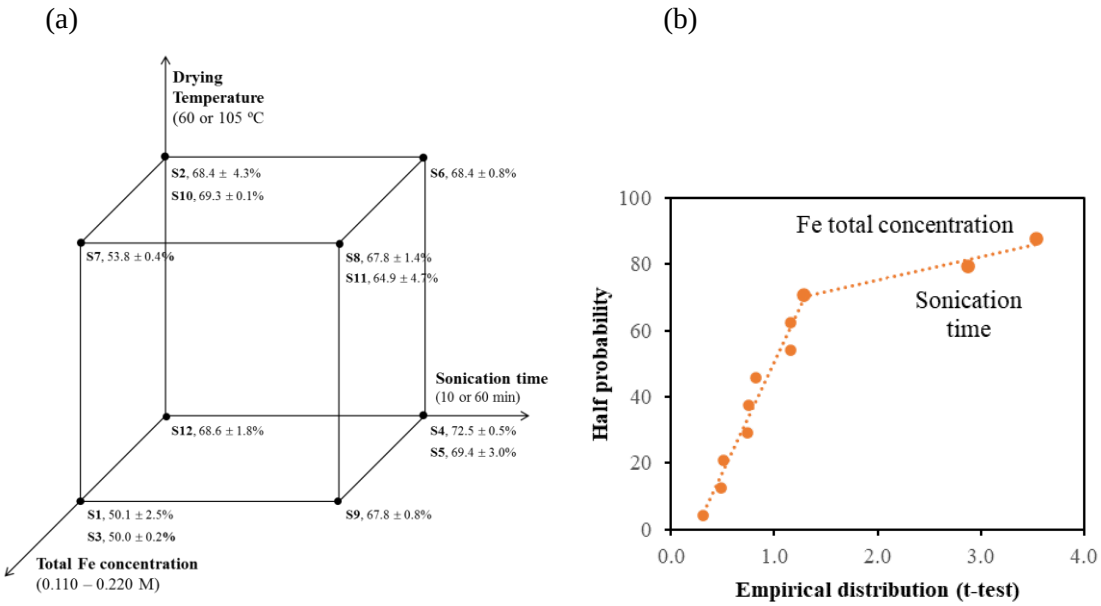

Fig. 1 (a) Average value of total iron measured by atomic absorption spectrometry, and (b) Half probability plot with half-probability as a function of the absolute value of the t-test.

3.2 FTIR spectra

In order to analyse the effect of the synthesis variables on the structural properties of the samples, FTIR spectroscopy was employed. Figure 2 shows the FTIR spectra of samples S3, S4, S8, and S10 in the wavenumber range 400 – 4000 cm^{-1}. These samples represent orthogonal experimental conditions in the fractional factorial design for the total initial concentration of Fe(III) and Fe(II) ions, sonication time and drying concentration (see Table 1 and Figure 1(a)).

Correlation analysis for the bands of higher intensity including the twelve samples of the experimental design (Table ESI2) revealed that there was a correlation higher than 0.90 for the bands that appeared at ~3388, ~3167, ~1402, ~1188, ~1090, and ~1009 cm^{-1}, which confirms that these bands result from different vibration modes including O-H bonds. The strong correlation among bands at ~731, ~634, ~588 and 438 cm^{-1} supports the assignation of these bands to vibration modes including Fe-O bonds. The correlation analysis for the samples also revealed that samples S1, S3 and S7 have similar structural characteristics, which differ from the other samples (Table ESI3**).**

For the most intense band between 500 and 700 cm^{-1}, the absorbance of samples S1, S3 and S7, which were synthesized from 0.220 mol L^{-1} total Fe and were sonicated for 10 min, was approximately three times lower than the absorbance of the rest of the samples. The fact that S1, S3 and S7 also had the lowest percentages of total iron corroborates that samples prepared from

0.220 mol L^{-1} Fe concentration had a larger percentage of Fe hydroxides and a lower content of Fe_3O_4 than the samples synthesized form a 0.110 mol L^{-1} Fe concentration.

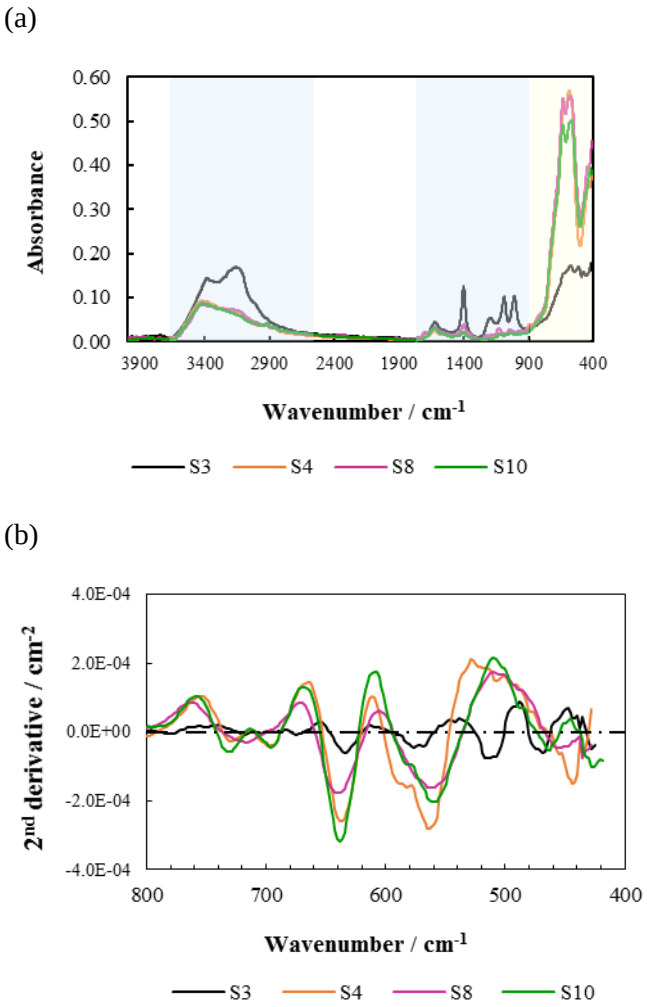

Fig. 2 (a) Infrared spectra of samples synthesized under orthogonal conditions according to experimental design. (b) Second derivative of the response in the 800 – 400 cm^{-1} wavenumber range.

The specific bands for ferrite appear in the region between 800 and 400 cm^{-1}, which are assigned to different vibrations modes of Fe-O bonds in the crystal lattice [25]. The maximum absorption in the spectra appears in a complex band between ~550 and ~650 cm^{-1}, which includes some overlapping of bands. We computed the finite differences in absorbance related to the wavenumber as an approximation of the actual second derivative (Fig. 2(b)) [26]. The plot of the second derivative as a function of the wavenumber reveals the presence of two vibration modes at ~560 and 633 cm^{-1}, which confirm the formation of magnetic nanoparticles

[27]. In particular, the band at ~560 cm^{-1} is assigned to Fe(III)-O stretching vibration inside the tetrahedral sites of inverse spinel structure [27].

The effect of the variables and the t-test for the absorbance at 633 cm^{-1} are included in Table ESI2. According to these results, increasing the sonication time from 10 to 60 min, as well as decreasing the Fe initial concentration from 0.220 mM to 0.110 mM and the ethanol content from 25 to 5%, favoured the crystallization of iron oxides, as it is demonstrated by the increase in the absorbance at ~633 cm^{-1}. It should be noted that the effect of sonication time was more pronounced for 0.220 mol L^{-1} Fe(III) than for 0.110 M. The fact that the value of t-test for variable dummy 2 exceeded 2.0 must be attributed to confounding. Furthermore, the normalized effects of the variables were plotted on a half normal probability scale (Fig. 3) similarly to the previous results of the final Fe content (see Fig. 1(b)). Therefore, the FTIR spectra confirm the results from the elemental analysis. A larger concentration of Fe ions increased the concentration of iron hydroxides. When sonication time increased from 10 to 60 minutes the iron oxyhydroxides gave off water and transformed into magnetite.

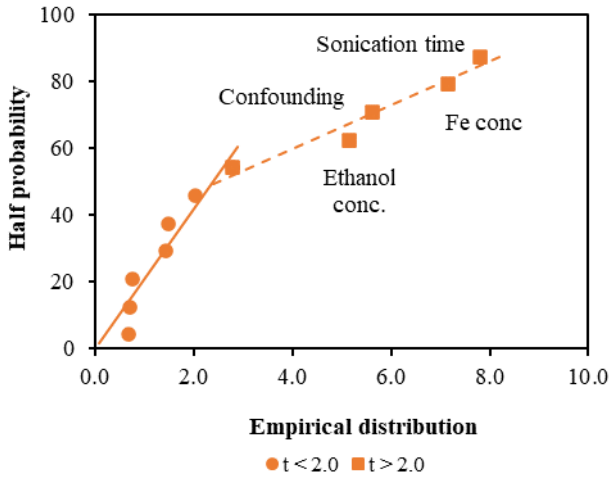

Fig. 3 Half probability plot for absorbance at 633 cm^{-1}. Sonication time, the concentration of Fe salts and the ethanol concentration significantly affected the absorbance of the 633 cm^{-1} band, which is related to the presence of magnetite.

The fact that the samples synthesized under 0.220 mol L^{-1} Fe and sonicated for 10 min (S1, S3 and S7) had higher absorbance for FeO-H stretching and bending bands in the 3500 – 900 cm^{-1} range may indicate that iron oxyhydroxides are first formed and that magnetite and maghemite evolved by dehydration and phase transformation [28, 29]. According to Baumgartner and Faivre, “For a thermodynamically controlled nucleation process, i.e. assuming fast diffusion and small nuclei, the firstly formed phase is the one with the lowest free energy barrier. When this phase is metastable with respect to the thermodynamically most stable phase and the energetic barriers for further transformations are low enough, stepwise transformation

that eventually yields the most stable phase instead of a single nucleation-growth event". In this case, iron oxyhydroxides that have lower surface energy than iron oxides are first precipitated.

3.3 X-Ray diffractograms

The twelve samples of the fractional factorial design were characterized by X-ray diffraction. As an example, Figure 4 shows the diffraction patterns of samples S3, S4, S8, and S10. All patterns include the characteristic peaks for magnetite (COD card n. 9007644), which appear at ~30.1 º, (220); ~35.4 º, (311); ~43.1 º, (400); ~52.5 º, (422); ~57.0 º, (511); ~62.5 º, (440); ~71.4 º, (620); ~74.5 º, (533); ~79.6 º, (622) [26]. However, the diffractogram from sample S3, and also for S1 and S7 that are not included in Fig. 4, has an unstable baseline and one additional peak at ~32.6 º (104), which is related to hematite (COD card n. 9000139) (the presence of other hematite-derived bidimensional phases like hematene cannot be disregarded [34, 35] and corroborate the differences found in the FTIR spectra.. Samples that were synthesized from 0.110 mol L^{-1} Fe presented sharper peaks than those prepared from 0.220 mol L^{-1} Fe. These results reinforce the hypothesis that for an initial 0.220 mol L^{-1} concentration of Fe, the coprecipitation of iron ions is governed by kinetic parameters more than by thermodynamics parameters [21]. Precipitation occurs first in the phase with the lowest free energy of Gibbs, which in the system is the iron oxyhydroxides [28, 29]. Fe(II) ions are incorporated into a Fe(II)-ferric hydrate and give rise to high electron mobility. According to Jolivet et al.[21] "The mixed valence material transforms with time into spinel via two simultaneous competing pathways: (i) solid state reaction with dehydration and spinel ordering at short range without particle size variation; (ii) dissolution of Fe(II)-Fe(III) complexes from the surface, followed by crystallization of spinel oxide (Ostwald ripening) that produces particle growth."

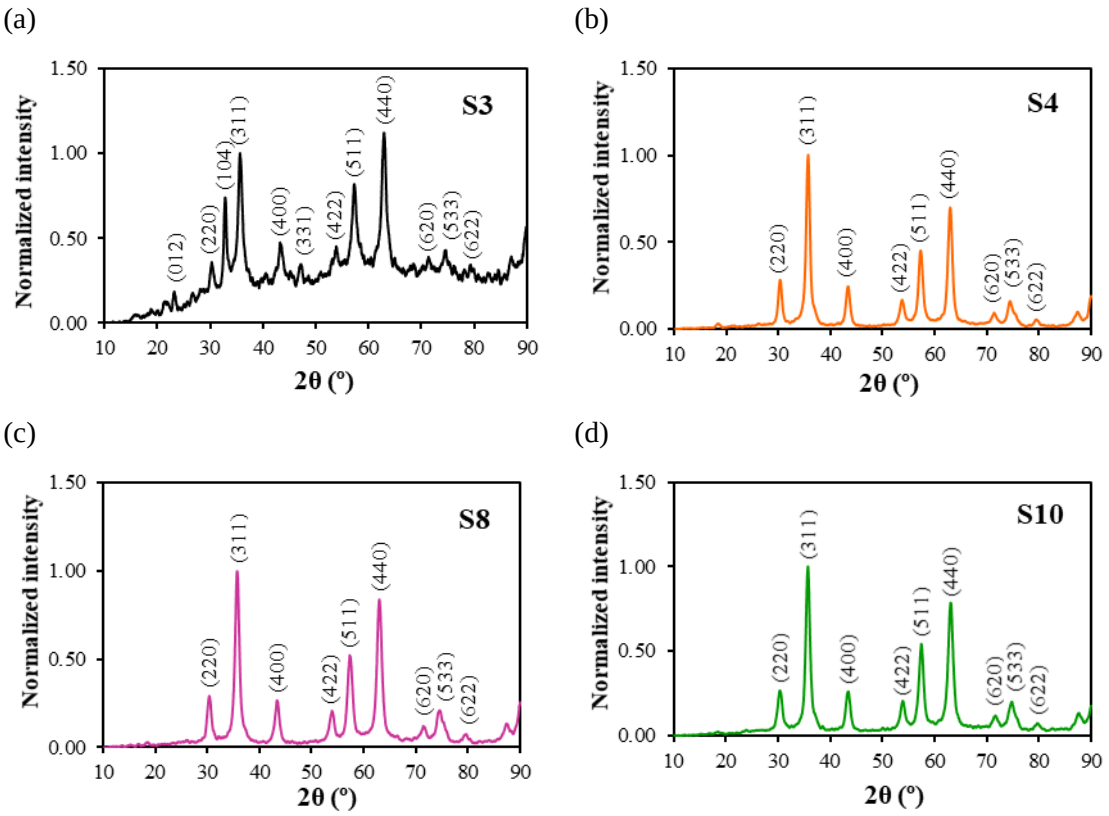

Fig. 4 XRD patterns of several samples that differed in the initial concentration of Fe, sonication time and drying temperature: (a) S3, (b) S4, (c) S8, and (d) S10. The intensity of the bands was normalized to the band at 35.4 º.

3.4 Particle morphology and size from High Resolution Transmission Electron Microscopy

Figure 5 shows high resolution transmission electron microscopy (HRTEM) images of samples S6, S7, S10 and S11, which also correspond to orthogonal points of the factorial design for total Fe concentration, sonication time and concentration of the aqueous ammonia solution (see Tables 1 and 2). The size distribution histograms for each synthesis condition are included in Figure ES1 of the Electronic Supplementary Information. The composition and morphology of the nanoparticles mainly depend on the initial concentration of iron salts, the sonication time and the ammonia concentration. For 0.110 mol L^{-1} Fe concentration and sonication for 60 min, the samples had a larger content of spheroid particles. Sample S6 is a good example of this type of nanoparticles, with an average size of 10.3 nm (Fig. 5(a)). Despite no size selection being applied to the as synthesized particles, the picture shows rather uniform size and shape. The samples synthesized from 0.220 mol L^{-1} Fe that were sonicated for 10 min include a mixture of spheroid and fibrillary nanoparticles (Fig. 5(b)). As an example, the image from sample S7

portrays aggregates of spheroidal nanoparticles, characteristic of magnetite and other fibroid or rod-like nanoparticles. The results from HRTEM also support the hypothesis that for 0.220 mol L^{-1} Fe total concentration, the reaction kinetics, in which the precipitation of oxyhydroxides is favoured, prevails over the thermodynamic constraints.

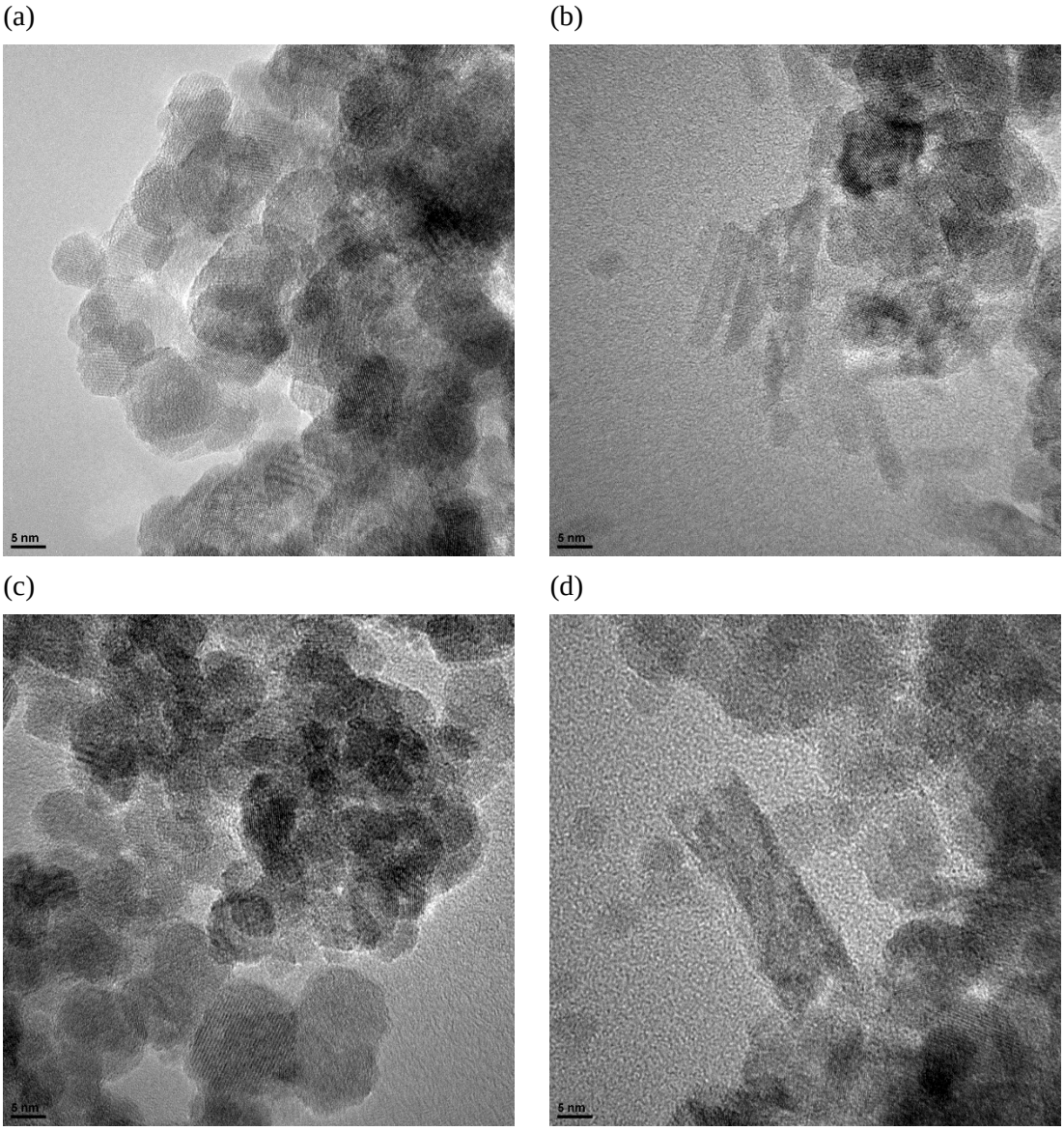

Fig. 5 HRTEM detail of iron nanoparticles: (a) S6, (b) S7, (c) S10, and (d) S11.

Table 3 includes average particle size with the limits of confidence obtained from TEM micrographs and XRD diffractograms (Scherrer equation) for samples S1 – S12 of the experimental design. Several TEM images were used for each sample to reduce bias in the measurement. The same primary particles were classified as “spheroid”, “ovoid”, “faceted”, or “rod-like”. In samples S1, S3 and S7, which were polyphasic, the-particles with a rod-like shape were not taken into account to work out the average size. The average particle size deduced

from TEM images varied from 5.9 ± 0.9 for S3 sample to 10.3 ± 1.3 for S6. In general, the average size estimated from the XRD data was similar to the values obtained from direct measurement from TEM images. For samples with lower crystallite size, average size from XRD data varied from 1.6 nm for S1 to 3.4 nm for S7.

Table 3 Average particle size with limits of confidence obtained from TEM micrographs and XRD diffractograms for samples S1 – S12 of the experimental design

Sample	**TEM Size /nm**			**XRD Size /nm**	**Difference / nm**
S6	10.3	±	1.3	7.8	2.5
S2	8.6	±	0.5	8.8	-0.2
S9	8.6	±	0.6	7.6	1.0
S4	8.2	±	0.6	8.2	0
S11	8.0	±	0.6	7.7	0.3
S5	7.7	±	0.3	7.0	0.7
S10	7.4	±	0.3	7.3	0.1
S7	7.1	±	0.5	3.4	3.7
S12	6.9	±	0.7	7.7	-0.8
S8	6.6	±	0.3	7.5	-0.9
S1	6.1	±	0.3	1.6	4.5
S3	5.9	±	0.9	2.6	3.3

Fig. 6(a) shows the average particle size from HRTEM in a three-dimension space that includes Fe concentration, sonication time and ammonia concentration. The effect of each variable on the particle size and the statistical significance t-test were calculated are included in Table ESI2. The dummy variables whose t-test value were < 2.0 were chosen for calculating the variance and the standard error. The fact that the t-test values for dummy variables four and five were 7.8 and 4.2, respectively, demonstrated confounding among the variables [18, 30]. In order to confirm the statistical analysis from t-test values, we plotted the t-values by using the Birnbaun's method of half probability, an empirical cumulative distribution method (Fig 6(b)). The variables E, B, D, C and F all fall on a straight line, with its origin passing through zero. The variables' sonication time, total Fe concentrations, ammonia concentrations, drying temperatures and dummies four and five deviate from the straight line passing through zero, denoting a significant variable effect.

(a) (b)

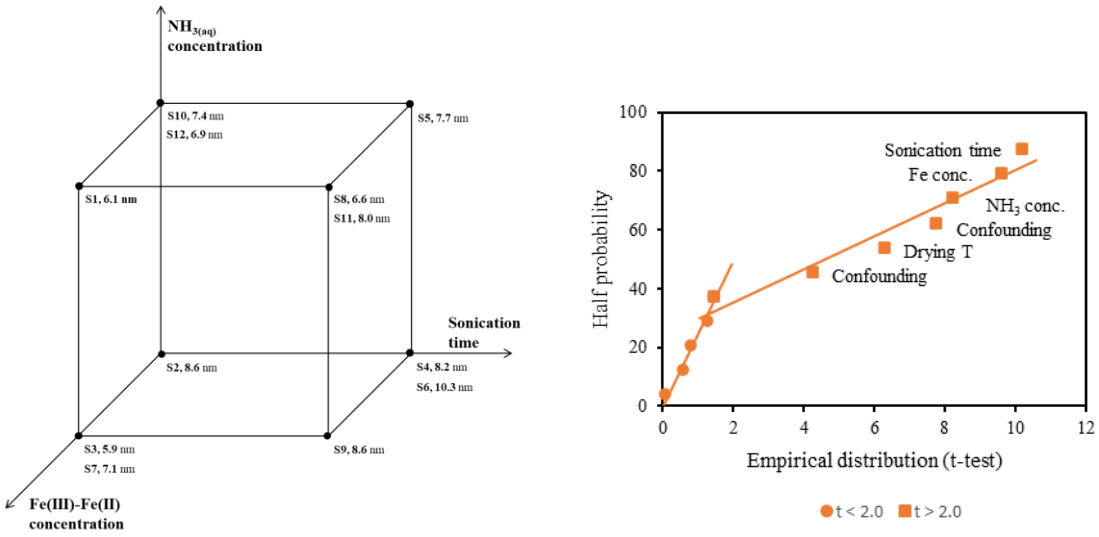

Fig. 6 (a) Particle size from HRTEM in a three-dimension space for Fe concentration (0.110 and 0.220 mol L^{-1}), sonication time (10 and 60 min) and ammonia concentration (0.90 and 1.2 mol L^{-1}); (b) Half probability as a function of the absolute value of the t-test.

The effect of the significant experimental variables on the average particle size can be explained according to the kinetics and thermodynamics of homogeneous nucleation. The critical nucleation radius (R*) increases with the molar volume (V_M) and the interfacial energy (γ_{S-L}), and decreases with the absolute temperature (T) and the natural logarithm of the saturation ratio (a/a_0).

$$R^* = \frac{2V_M\gamma_{S-L}}{kT\ \ln\left(\frac{a}{a_0}\right)}$$

Therefore, increasing the total Fe concentration and the ammonia concentration will increase supersaturation, which will result in smaller crystallites. If the nuclei are smaller than a one-unit cell, the growing crystallites initially produced will tend to precipitate as an amorphous gel. S1, S3 and S7 samples, which were synthesized from a 0.220 mol L^{-1} Fe concentration and sonicated for 10 min, yielded polyphasic systems that contained mixtures of Fe-oxyhydroxides and magnetic nanoparticles with the lowest average particle size. For a given total Fe and ammonia concentration, average particle size increased with sonication. For example, we can compare average values for S2 and S6 (8.6 and 10.3 nm, respectively) with values for S3 (5.9 nm) with S9 (8.6 nm). According to the classic theory for homogenous nucleation and the initiation and formation of the solid-phase, the initial conditions govern the pathways. Ions can accrete to form the less stable amorphous or crystalline nucleus. When two phases compete for the same dissolved ions, the amorphous phase, which has a lower energy barrier than the crystalline one, will be favoured because the rate of nucleation is related to the change in free

energy. Crystalline magnetite competes with a metastable phase of iron oxyhydroxides [28]. Initial conditions such as 110 mM total Fe initial concentration and 0.90 mol L^{-1} ammonia concentration reduce supersaturation and enhance the nucleation of crystalline magnetite with a higher critical radius of the nuclei. Increasing sonication time from 10 to 60 min and the drying temperature from 60 to 105 ºC promote a solid-state transformation of oxyhydroxides to crystalline magnetite and crystal growth.

3.5 Specific Absorption Rate (SAR)

Figure 7 shows the measured specific absorption rate (SAR) of the samples as a function of the applied AC magnetic field intensity. Depending on the measured SAR values, the samples can be classified into three different groups. The first group, here referred to as Group I, is composed of sample S4 and S6, which had the highest SAR values. A second group, composed of S12, S2, S9, S5, S10, S11 and S12, includes samples with intermediate SAR values. Finally, a third group, called here Group III, is composed of S1, S3 and S7, which have the lowest SAR values. The slope of SAR with respect to magnetic field intensity is much larger for Group I than for Groups II and III. In other words, the SAR increases much faster with magnetic field intensity in the case of samples S4 and S6 than it does in the case of the other samples. Although S2 belongs to Group II, its slope of SAR with respect to magnetic field intensity is close to the slopes from Group I.

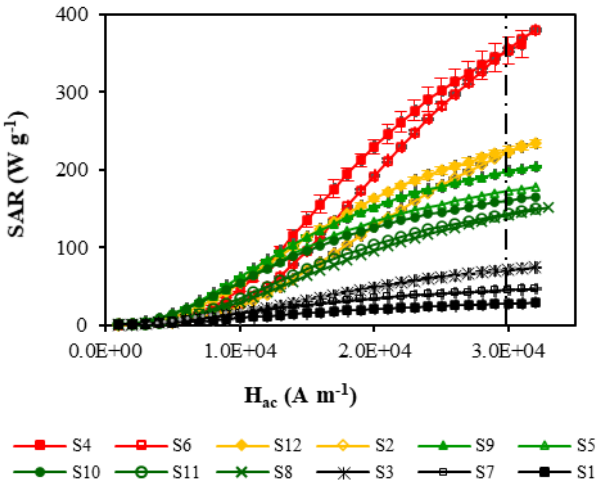

Fig. 7 Specific absorption rate (SAR) as a function of the applied AC magnetic field intensity. The applied field frequency was 284 kHz. The error bars were estimated from the standard deviation when repeating the measurement process four times.

In order to carry out the factorial design, the SAR was evaluated at 30 kA/m (308 Oe) field intensity. These SAR values varied from 28 Wg^{-1} (for sample S1) to 355 Wg^{-1} (for S6). The variance was 182 W g^{-1} and the standard error estimated from the five dummies variable was 13.5 W g^{-1}. The t-test for the experimental variables showed that the total Fe concentration (t-test = 5.32), the sonication time (t-test = 3.78) and the ammonia concentration (t-test = 2.32) significantly affected the SAR (Table ESI2). The largest absorption rate values were obtained when the total Fe concentration was 0.110 M, the ammonia concentration was 0.90 M, and the samples were sonicated for 60 min.

Considering the different characterization techniques, the trends in measured SAR values match the other properties discussed before. Samples S1, S3 and S7 from Group III with the lower SAR values correspond to the samples with greater absorbance in FTIR spectra for FeO-H stretching and bending bands, which indicate the presence of iron oxyhydroxides (Section 3.2). In addition, X- ray diffractograms for samples S1, S3 and S7 show additional peaks related to the presence of ferrihydrites. Therefore, samples S1, S3 and S7 are polyphasic and hence have lower intrinsic magnetization, which results in a lower SAR [6]. The remaining samples from group I and II, on the other hand, are largely monophasic and, hence, they present larger SAR values than the samples containing oxyhydroxides.

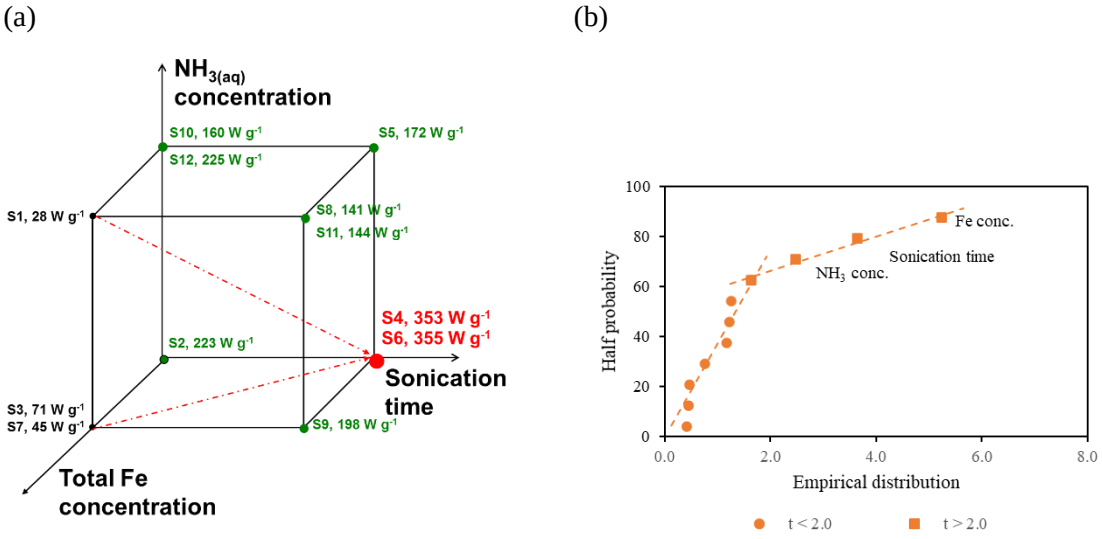

Fig. 8 (a) Specific absorption rate (SAR) in a three-dimension space for Fe concentration (0.110 and 0.220 mol L^{-1}), sonication time (10 and 60 min) and ammonia concentration (0.90 and 1.2 mol L^{-1}); (b) Birnaun plot with half probability as a function of the absolute value of the t-test.

The remaining samples from Groups I and II all have similar phase purities and so they could be expected to have similar intrinsic magnetizations and SARs. However, the SARs of samples S4 and S6 from Group I vary with magnetic field intensity, like large size iron oxide

nanoparticles: below a threshold magnetic field intensity the SAR is small and negligible, whereas above that threshold intensity it sharply increases. This behaviour has been theoretically predicted [31] and reported in the literature for chemically synthetized particles [32] and for magnetosomes [33]. According to the TEM images (Section 3.4), the larger particle diameters correspond to S2, S4, S6 and S9. Therefore, there is a correspondence between the MNPs sizes obtained by TEM and the SAR values. However, there are some, albeit rather small, discrepancies. Although S9 has a large TEM size, it belongs to Group II. This can be explained by its lower size obtained by X-ray diffraction (Section 3.3), which is slightly lower than S6 and S4. The sample labelled S2, on the other hand, has a smaller SAR (group II), although the slope of SAR with respect to field intensity is analogous to Group I. The differences in the coercive fields, due to different effective anisotropies [31] of the samples, could lead to the mentioned discrepancies in SAR values.

Conclusions

The experimental results from a Plackett – Burman factorial design at two levels for analysing the simultaneous effect of total Fe concentration, ammonia concentration, reaction temperature, sonication time and percentage of ethanol in aqueous reaction media leads to the conclusion that total iron concentration and sonication time steered the overall reaction mechanism, as well as the composition, crystallinity, size and morphology of iron oxide nanoparticles that, in turn, determine the specific absorption for hyperthermia. An initial solution made up of 0.110 mol L^{-1} total Fe and either 0.90 or 1.20 mol L^{-1} $NH_{3(aq)}$ led to the formation of magnetite nanoparticles. When the initial concentration of Fe was 0.220 mol L^{-1}, kinetics prevailed over thermodynamics during nucleation and a metastable phase of iron oxyhydroxides precipitated together with magnetite. Sonication of the reaction media promoted a phase transformation of metastable phases to magnetite, and also the development of crystallinity and Ostwald ripening.

Acknowledgements

P. Moriones is grateful to the “Departamento de Industria y Tecnología, Comercio y Trabajo” of the Navarre Goverment (Spain) for the fellowships granted (Ref. number 175/01/08 and 269/01/08, respectively). L. Cervera acknowledges Public University of Navarre for her Ph.D contract "Contratos Pre-doctorales adscritos a Grupos e Institutos de Investigación de la Universidad Pública de Navarra". The authors thank Alfonso Ibarra from the “Instituto de Nanociencia de Aragón” Spain for the HRTEM analysis.

References

[1] L. Pourtau, H. Oliveira, J. Thevenot, Y.L. Wan, A.R. Brisson, O. Sandre, S. Miraux, E. Thiaudiere, S. Lecommandoux, Antibody-Functionalized Magnetic Polymersomes: In vivo Targeting and Imaging of Bone Metastases using High Resolution MRI, Adv Healthc Mater, 2 (2013) 1420-1424.

[2] I. Koh, L. Josephson, Magnetic Nanoparticle Sensors, Sensors, 9 (2009) 8130-8145.

[3] R. Dalpozzo, Magnetic nanoparticle supports for asymmetric catalysts, Green Chemistry, 17 (2015) 3671-3686.

[4] A. Jordan, P. Wust, H. Fahling, W. John, A. Hinz, R. Felix, Inductive heating of ferrimagnetic particles and magnetic fluids - Physical evaluation of their potential for hyperthermia, International Journal of Hyperthermia, 9 (1993) 51-68.

[5] J.-P. Fortin, C. Wilhelm, J. Servais, C. Menager, J.-C. Bacri, F. Gazeau, Size-sorted anionic iron oxide nanomagnets as colloidal mediators for magnetic hyperthermia, Journal of the American Chemical Society, 129 (2007) 2628-2635.

[6] R.E. Rosensweig, Heating magnetic fluid with alternating magnetic field, J. Magn. Magn. Mater., 252 (2002) 370-374.

[7] R. Hergt, S. Dutz, Magnetic particle hyperthermia-biophysical limitations of a visionary tumour therapy, J. Magn. Magn. Mater., 311 (2007) 187-192.

[8] I. Castellanos-Rubio, M. Insausti, E. Garaio, I.G. de Muro, F. Plazaola, T. Rojo, L. Lezama, Fe3O4 nanoparticles prepared by the seeded-growth route for hyperthermia: electron magnetic resonance as a key tool to evaluate size distribution in magnetic nanoparticles, Nanoscale, 6 (2014) 7542-7552.

[9] A.H. Lu, E.L. Salabas, F. Schuth, Magnetic nanoparticles: Synthesis, protection, functionalization, and application, Angew Chem Int Edit, 46 (2007) 1222-1244.

[10] S. Laurent, D. Forge, M. Port, A. Roch, C. Robic, L.V. Elst, R.N. Muller, Magnetic iron oxide nanoparticles: Synthesis, stabilization, vectorization, physicochemical characterizations, and biological applications, Chem. Rev., 108 (2008) 2064-2110.

[11] W. Wu, Z.H. Wu, T. Yu, C.Z. Jiang, W.S. Kim, Recent progress on magnetic iron oxide nanoparticles: synthesis, surface functional strategies and biomedical applications, Science and Technology of Advanced Materials, 16 (2015).

[12] J.-P. Jolivet, E. Tronc, C. Chaneac, Iron oxides: From molecular clusters to solid. A nice example of chemical versatility, Comptes Rendus Geoscience, 338 (2006) 488-497.

[13] C. Blanco-Andujar, D. Ortega, Q.A. Pankhurst, N.T.K. Thanh, Elucidating the morphological and structural evolution of iron oxide nanoparticles formed by sodium carbonate in aqueous medium, J. Mater. Chem., 22 (2012) 12498-12506.

[14] H.N. Meng, Z.Z. Zhang, F.X. Zhao, T. Qiu, J.D. Yang, Orthogonal optimization design for preparation of Fe3O4 nanoparticles via chemical coprecipitation, Applied Surface Science, 280 (2013) 679-685.

[15] D. Bonvin, H. Hofmann, M.M. Ebersold, Optimisation of aqueous synthesis of iron oxide nanoparticles for biomedical applications, J. Nanopart. Res., 18 (2016).

[16] M.R. Ghazanfari, M. Kashefi, M.R. Jaafari, Optimizing and modeling of effective parameters on the structural and magnetic properties of Fe3O4 nanoparticles synthesized by coprecipitation technique using response surface methodology, J. Magn. Magn. Mater., 409 (2016) 134-142.

[17] A. Asfaram, M. Ghaedi, S. Hajati, A. Goudarzi, E.A. Dil, Screening and optimization of highly effective ultrasound-assisted simultaneous adsorption of cationic dyes onto Mn-doped Fe3O4-nanoparticle-loaded activated carbon, Ultrason. Sonochem., 34 (2017) 1-12.

[18] K. Jones, Optimization of experimental data, International Laboratory, 16 (1986) 32-45.

[19] R. Massart, Preparation of Aqueous Magnetic Liquids in Alkaline and Acidic Media, Ieee Transactions on Magnetics, 17 (1981) 1247-1248.

[20] J.P. Jolivet, P. Belleville, E. Tronc, J. Livage, Influende of Fe(II) on the formation of the spinel iron-oxide in alkaline-medium, Clays Clay Miner., 40 (1992) 531-539.

[21] J.P. Jolivet, E. Tronc, C. Chaneac, Synthesis of iron oxide-based magnetic nanomaterials and composites, Comptes Rendus Chimie, 5 (2002) 659-664.

[22] H. Mark, J. Workman, Derivatives in spectroscopy Part I - The behavior of the derivative, Spectroscopy, 18 (2003) 32-37.

[23] H. Mark, J. Workman, Derivatives in spectroscopy Part II - The true derivative, Spectroscopy, 18 (2003) 25-28.

[24] E. Garaio, J.M. Collantes, J.A. Garcia, F. Plazaola, S. Mornet, F. Couillaud, O. Sandre, A wide-frequency range AC magnetometer to measure the specific absorption rate in nanoparticles for magnetic hyperthermia, J. Magn. Magn. Mater., 368 (2014) 432-437.

[25] R.D. Waldron, Infrared spectra of ferrites, Physical Review, 99 (1955) 1727-1735.

[26] M. Stoia, R. Istratie, C. Pacurariu, Investigation of magnetite nanoparticles stability in air by thermal analysis and FTIR spectroscopy, J. Therm. Anal. Calorim., 125 (2016) 1185-1198.

[27] S. Li, T. Zhang, R. Tang, H. Qiu, C. Wang, Z. Zhou, Solvothermal synthesis and characterization of monodisperse superparamagnetic iron oxide nanoparticles, J. Magn. Magn. Mater., 379 (2015) 226-231.

[28] J. Baumgartner, A. Dey, P.H.H. Bomans, C. Le Coadou, P. Fratzl, N.A.J.M. Sommerdijk, D. Faivre, Nucleation and growth of magnetite from solution, Nat Mater, 12 (2013) 310-314.

[29] J. Baumgartner, D. Faivre, Iron solubility, colloids and their impact on iron (oxyhydr)oxide formation from solution, Earth-Sci Rev, 150 (2015) 520-530.

[30] G.E.P. Box, W. Hunter, G., S.J. Hunter, Statistics for experimenters, John Wiley & Sons, New York, 1978.

[31] J. Carrey, B. Mehdaoui, M. Respaud, Simple models for dynamic hysteresis loop calculations of magnetic single-domain nanoparticles: Application to magnetic hyperthermia optimization, J. Appl. Phys., 110 (2011).

[32] G. Hemery, A.C. Keyes, Jr., E. Garaio, I. Rodrigo, J. Angel Garcia, F.P. La, E. Garanger, O. Sandre, Tuning Sizes, Morphologies, and Magnetic Properties of Monocore Versus Multicore Iron Oxide Nanoparticles through the Controlled Addition of Water in the Polyol Synthesis, Inorg. Chem., 56 (2017) 8232-8243.

[33] A. Muela, D. Munoz, R. Martin-Rodriguez, I. Orue, E. Garaio, A. Abad Diaz de Cerio, J. Alonso, J. Angel Garcia, M. Luisa Fdez-Gubieda, Optimal Parameters for Hyperthermia Treatment Using Biomineralized Magnetite Nanoparticles: Theoretical and Experimental Approach, J. Phys. Chem. C, 120 (2016) 24437-24448.

[34] Puthirath Balan, A., Radhakrishnan, S., Woellner, C.F. et al. Exfoliation of a non-van der Waals material from iron ore hematite. Nature Nanotech 13, 602–609 (2018).

[35] Zhang, B.Y., Xu, K., Yao, Q. *et al.* Hexagonal metal oxide monolayers derived from the metal–gas interface. *Nat. Mater.* (2021).